



## Ion-gel-gating-induced oxygen vacancy formation in epitaxial $\text{La}_{0.5}\text{Sr}_{0.5}\text{CoO}_{3-\delta}$ films from *in operando* x-ray and neutron scattering

Jeff Walter,<sup>1</sup> Guichuan Yu,<sup>2</sup> Biqiong Yu,<sup>2</sup> Alexander Grutter,<sup>3</sup> Brian Kirby,<sup>3</sup> Julie Borchers,<sup>3</sup> Zhan Zhang,<sup>4</sup> Hua Zhou,<sup>4</sup> Turan Birol,<sup>1</sup> Martin Greven,<sup>2</sup> and Chris Leighton<sup>1,\*</sup>

<sup>1</sup>Department of Chemical Engineering and Materials Science, University of Minnesota, Minneapolis, Minnesota 55455, USA

<sup>2</sup>School of Physics and Astronomy, University of Minnesota, Minneapolis, Minnesota 55455, USA

<sup>3</sup>NIST Center for Neutron Research, National Institute of Standards and Technology, Gaithersburg, Maryland 20899, USA

<sup>4</sup>Advanced Photon Source, Argonne National Laboratory, Argonne, Illinois 60439, USA

(Received 10 October 2017; published 19 December 2017)

Ionic-liquid/gel-based transistors have emerged as a potentially ideal means to accumulate high charge-carrier densities at the surfaces of materials such as oxides, enabling control over electronic phase transitions. Substantial gaps remain in the understanding of gating mechanisms, however, particularly with respect to charge carrier vs oxygen defect creation, one contributing factor being the dearth of experimental probes beyond electronic transport. Here we demonstrate the use of synchrotron hard x-ray diffraction and polarized neutron reflectometry as *in operando* probes of ion-gel transistors based on ferromagnetic  $\text{La}_{0.5}\text{Sr}_{0.5}\text{CoO}_{3-\delta}$ . An asymmetric gate-bias response is confirmed to derive from electrostatic hole accumulation at negative gate bias vs oxygen vacancy formation at positive bias. The latter is detected via a large gate-induced lattice expansion (up to 1%), complementary bulk measurements and density functional calculations enabling *quantification* of the bias-dependent oxygen vacancy density. Remarkably, the gate-induced oxygen vacancies proliferate through the entire thickness of 30–40-unit-cell-thick films, quantitatively accounting for changes in the magnetization depth profile. These results directly elucidate the issue of electrostatic vs redox-based response in electrolyte-gated oxides, also demonstrating powerful approaches to their *in operando* investigation.

DOI: [10.1103/PhysRevMaterials.1.071403](https://doi.org/10.1103/PhysRevMaterials.1.071403)

Electrolyte gating using ionic liquids and gels in electric double-layer transistors (EDLTs) is emerging as a premier approach for the study and manipulation of carrier-density-controlled phenomena [1,2]. The nanoscopic EDL formed by the electrolyte cations (anions) and induced surface electrons (holes) results in very large capacitance (up to  $\sim 100 \mu\text{F cm}^{-2}$ ) [3–5], inducing carrier densities exceeding  $10^{14} \text{ cm}^{-2}$  [4–9]. This is sufficient to control electronic and magnetic phase transitions [6–15], map phase behavior [12,13], and explore transport limits in semiconductors (e.g., [4,5,13,16–19]). The electric fields in the EDLs are so large, however ( $\sim 10 \text{ MV cm}^{-1}$ ), that mechanisms other than electrostatic carrier accumulation become possible. This is particularly important in transition-metal oxides, where electrolyte gating is being extensively explored. Superconductivity was discovered, for instance, in electrolyte-gated  $\text{KTaO}_3$  [6], and controlled in  $\text{SrTiO}_3$  [10] and cuprates [11,12]. Metal-insulator transitions have been similarly controlled in  $\text{VO}_2$  [14,20,21] and nickelates [7,15], while ferromagnetism has been modulated in  $\text{Ti}_{1-x}\text{Co}_x\text{O}_2$  [8],  $\text{La}_{1-x}\text{Sr}_x\text{MnO}_3$  [9], and  $\text{La}_{1-x}\text{Sr}_x\text{CoO}_{3-\delta}$  [22]. It is increasingly apparent, however, that the gate response in oxides can be electrochemical rather than electrostatic, the electric field in the EDL inducing redox in the oxide, particularly via oxygen vacancy ( $V_{\text{O}}$ ) formation. Evidence for bias-induced  $V_{\text{O}}$  creation has been gathered from controlled atmosphere transport and tracer experiments in  $\text{VO}_2$  [23],  $\text{SrTiO}_3$  [24], and  $\text{TiO}_2$  [25], although controversy remains, particularly in  $\text{VO}_2$  [14,26].

Recent work of ours on ion-gel-gated  $\text{La}_{0.5}\text{Sr}_{0.5}\text{CoO}_{3-\delta}$  (LSCO) films provided insight into this issue of electrostatics

vs electrochemistry by uncovering clear asymmetry with respect to gate-bias ( $V_{\text{g}}$ ) polarity [22]. While electrostatic hole accumulation was deduced at negative  $V_{\text{g}}$  in this *p*-type oxide,  $V_{\text{O}}$  formation was implicated at positive  $V_{\text{g}}$ , from transport [22]. This was interpreted in terms of the known redox stability of LSCO, similar to many oxides, where  $V_{\text{O}}$  creation is thermodynamically preferred to  $V_{\text{O}}$  annihilation. At positive  $V_{\text{g}}$ ,  $V_{\text{O}}$  formation is thus favored over hole depletion, while at negative  $V_{\text{g}}$  hole accumulation is favored over  $V_{\text{O}}$  annihilation [22]. This could indicate that *n*-type oxides such as  $\text{VO}_2$ , which require EDLT operation at  $V_{\text{g}} > 0$  (at least for undoped materials), could be particularly prone to  $V_{\text{O}}$  formation. Such explanations are attractive, but require further testing. In addition, recent work has placed further emphasis on  $V_{\text{g}}$ -induced ionic motion by uncovering electrochemical hydrogen incorporation in  $\text{WO}_3$  [27] and  $\text{SrCoO}_{2.5}$  [28]. There are thus several emerging control concepts in oxide EDLTs, further work being needed to untangle mechanisms.

One impediment to improved understanding of electrolyte gating is the dearth of available probes beyond electronic transport. The latter is dominant in the field, other more direct probes, such as spectroscopy and scattering, being challenging to implement in EDLTs. Difficulties include the small volume of gated material, and the thick overlying ion gel or ionic liquid, which induce absorption and scattering. Few demonstrations of *in operando* scattering or spectroscopy of electrolyte-gated oxides have thus appeared, although this now appears to be changing. Synchrotron x-ray diffraction (SXRD) results on ionic-liquid-gated  $\text{VO}_2$  [26],  $\text{La}_{2-x}\text{Sr}_x\text{CuO}_4$  [29],  $\text{SrCoO}_{2.5}$  [28],  $\text{WO}_3$  [27], and  $\text{NdNiO}_3$  [30] have recently appeared, along with x-ray absorption on  $\text{YBa}_2\text{Cu}_3\text{O}_{7-x}$  [31] and  $\text{NdNiO}_3$  [30]. Noteworthy findings emerge from these studies, including giant  $V_{\text{g}}$ -induced lattice expansion in  $\text{VO}_2$

\*Corresponding author: leighton@umn.edu

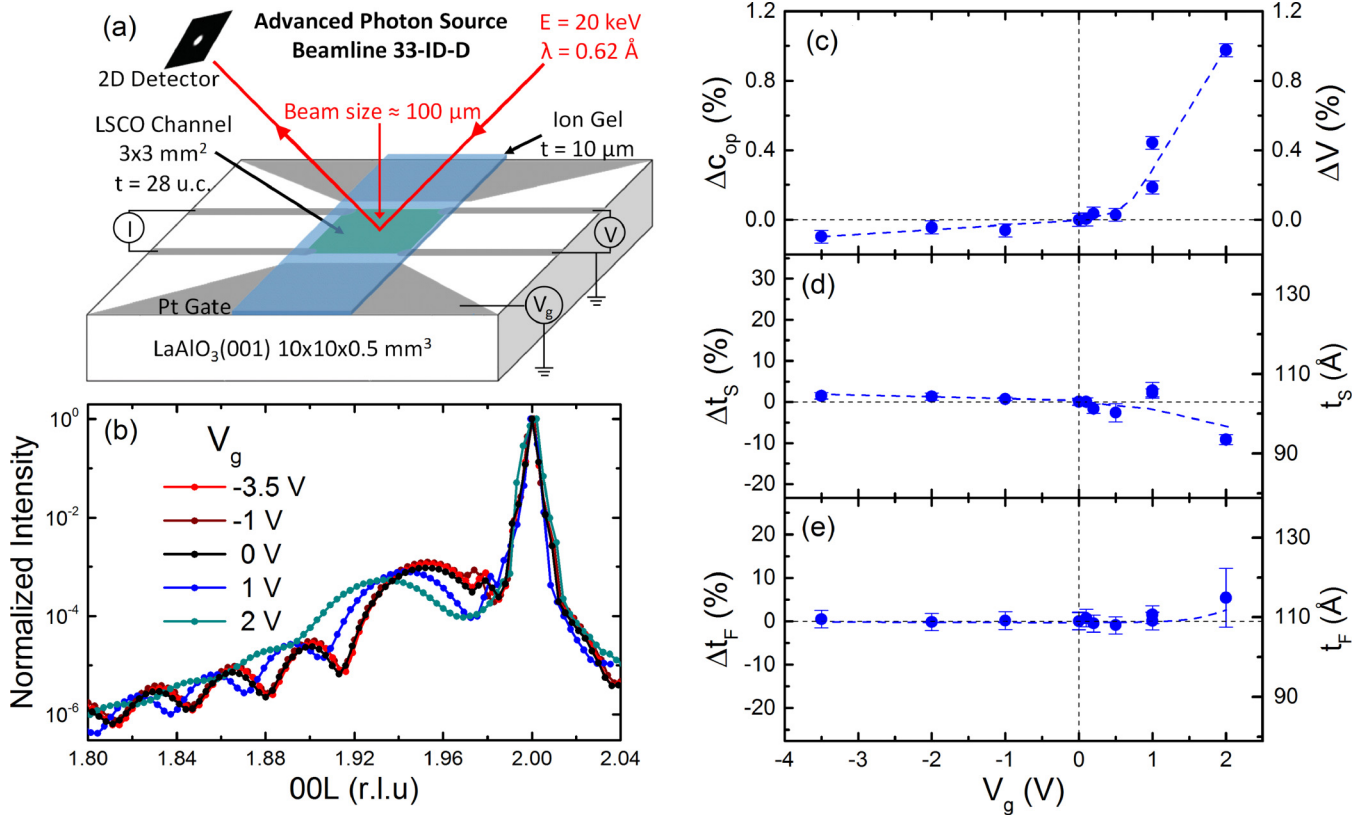


FIG. 1. (a) Device and experimental setup schematic for synchrotron x-ray diffraction on epitaxial  $\text{La}_{0.5}\text{Sr}_{0.5}\text{CoO}_{3-\delta}$  films. (b) Gate-bias ( $V_g$ )-dependent specular diffraction (00L) scans, where  $L$  is in reciprocal lattice units (r.l.u.) of the LAO substrate. (c) Change in  $c$ -axis lattice parameter ( $\Delta c_{\text{op}}$ , left axis) and cell volume ( $\Delta V$ , right axis) with  $V_g$ . (d) Change in Scherrer thickness ( $\Delta t_s$ , left axis), and  $t_s$  itself (right axis), vs  $V_g$ . (e) Change in film thickness from Laue fringes ( $\Delta t_f$ ), and  $t_f$  itself (right axis), vs  $V_g$ . Blue dotted lines are guides to the eye.

[26], deoxygenation of  $\text{YBa}_2\text{Cu}_3\text{O}_{7-x}$  under positive  $V_g$  [31], three-phase switching of  $(\text{H})\text{SrCoO}_{3-\delta}$  [28], and gate-bias polarity asymmetry (similar to LSCO [22]) in  $\text{NdNiO}_3$  [30]. *In operando* probes have thus yielded substantial insight, and additional work is clearly desirable, particularly with techniques capable of detecting  $V_{\text{O}}$  formation quantitatively, with spatial resolution.

In this work we demonstrate application of both SXRD and polarized neutron reflectometry (PNR) as *in operando* probes of epitaxial LSCO EDLTs, utilizing the penetration of hard x rays and neutrons. SXRD reveals only a small ( $<0.1\%$ ) decrease in the out-of-plane lattice parameter under negative  $V_g$ , compared to a large increase at positive  $V_g$  (up to 1% at +2 V). Complementary bulk powder XRD (PXRD) and thermogravimetric analysis (TGA) confirm that such lattice expansion is consistent with  $V_{\text{O}}$  formation, reproduced by density functional theory (DFT). The cell volume dependence on oxygen deficiency is then used to “calibrate” *in operando* SXRD, enabling *quantification* of the  $V_g$ -dependent  $V_{\text{O}}$  density, which reaches  $\delta = 0.16$  at +2 V. Importantly, SXRD indicates that these  $V_{\text{O}}$ 's proliferate through the entire thickness of  $\sim 30$ -unit-cell-thick films. This is confirmed by  $V_g$ -dependent PNR, the suppressed magnetization extending through the whole film, in *quantitative* agreement with the determined O deficiency. These results not only advance our understanding of gating mechanisms in oxide EDLTs, but

demonstrate powerful approaches to *in operando* structural and magnetic studies.

Details on film growth, device fabrication, *in operando* measurements, and bulk measurements/calculations are provided in Supplemental Material Secs. A–E (Figs. S1–S3) [32]. Briefly, epitaxial LSCO was deposited on  $\text{LaAlO}_3(001)$  (LAO) using high-pressure oxygen sputtering [22] and then thoroughly characterized [33–36]. Bulklike metallic ferromagnetism with Curie temperature,  $T_C \approx 220$  K was obtained above seven unit-cell thicknesses. EDLTs employing  $\sim 10$ - $\mu\text{m}$ -thick “cut and stick” ion gels [3] [see Fig. 1(a)] were then fabricated from these films. SXRD [Fig. 1(a)] was performed on the 33-ID beamline of the Advanced Photon Source, with 20 keV ( $\lambda = 0.62 \text{ \AA}$ ) radiation. Beam damage was reduced to negligible levels via procedures discussed in Supplemental Material Sec. B (Fig. S2) [32]. PNR was performed on the Polarized Beam Reflectometer at the NIST Center for Neutron Research (Supplemental Material Sec. C [32]), using a monochromated ( $4.75 \text{ \AA}$ ) neutron beam, at 30 K, in a saturating 3 T in-plane magnetic field ( $B$ ), and refinement was done with REFLID [37]. For both SXRD and PNR, devices were operated in vacuum ( $<10^{-5}$  mmHg),  $V_g$  being applied at 280–290 K for 30 min, with *in situ* monitoring of electrical transport. Complementary TGA in 1 bar of flowing  $\text{N}_2$  was performed on *bulk* LSCO (Supplemental Material Sec. D [32]). DFT+ $U$  calculations were performed using the Vienna

*ab initio* Simulation Package [38,39], using methods described in Supplemental Material Sec. E [32].

Starting with *in operando* SXRD, Fig. 1(b) displays specular 00L scans around the 002 LAO substrate reflection, at  $V_g = -3.5, -1, 0, 1,$  and  $2$  V. As shown in Supplemental Material Fig. S2(c) [32], no ion-gel-induced changes were observed prior to  $V_g$  application. The  $V_g = 0$  scan is typical of LAO(001)/LSCO [35,40]: a well-defined LSCO peak occurs at  $L = 1.95$ , corresponding to out-of-plane lattice parameter  $c_{op} = 3.89$  Å, surrounded by Laue oscillations. As expected for a fully strained film with negligible microstrain (Supplemental Material Sec. A, Fig. S1 [32]), the Scherrer length from the film peak width ( $t_s = 103 \pm 6$  Å) and the thickness from the oscillation spacing ( $t_f = 109 \pm 7$  Å) are in agreement with the thickness from x-ray reflectometry prior to gel application ( $t = 110 \pm 5$  Å, i.e., 28 unit cells). When gating is performed, negative  $V_g$  [e.g.,  $-1$  or  $-3.5$  V in Fig. 1(b)] results in only small changes in the 002 LSCO peak. For positive  $V_g$ , however, the situation is different: the LSCO reflection rapidly shifts to lower  $L$ , and the Laue oscillations become less prominent, indicating increased roughness/structural disorder. These changes are summarized in Figs. 1(c)–1(e), which shows

the  $V_g$  dependence of the  $c$ -axis lattice parameter shift ( $\Delta c_{op}$ ), Scherrer length shift ( $\Delta t_s$ ), and fringe spacing thickness shift ( $\Delta t_f$ ). The right axes show the cell volume change ( $\Delta V$ ) and absolute  $t_s$  and  $t_f$ , respectively. From Fig. 1(c), the asymmetry with respect to  $V_g$  polarity is striking. Negative  $V_g$  up to  $-3.5$  V results in a  $c_{op}$  decrease of  $<0.1\%$  (roughly linear in  $V_g$ ), whereas  $V_g = +2$  V induces a large (nonlinear) 1% lattice expansion. As shown in Figs. 1(d) and 1(e), this shift in  $c_{op}$  is accompanied by barely any variation in  $t_s$  and  $t_f$ , the only evidence of a statistically significant change occurring in  $t_s$  at  $+2$  V (see Supplemental Material Sec. F [32] for further discussion). This indicates, as can be seen from Fig. 1(b), that the LSCO film peak and Laue oscillations are uniformly shifted to lower  $L$  at positive  $V_g$ , with no significant broadening or peak splitting. This suggests that the positive-bias-induced lattice expansion occurs through the entire thickness of these 28-unit-cell films. In these measurements, which were performed in vacuum, the increase in  $c_{op}$  at positive  $V_g$  is irreversible (Supplemental Material Sec. F, Fig. S4) [32].

As discussed above, earlier transport studies on LSCO revealed similarly asymmetric  $V_g$  response, ascribed to  $V_O$  formation at positive bias, and electrostatic hole accumulation

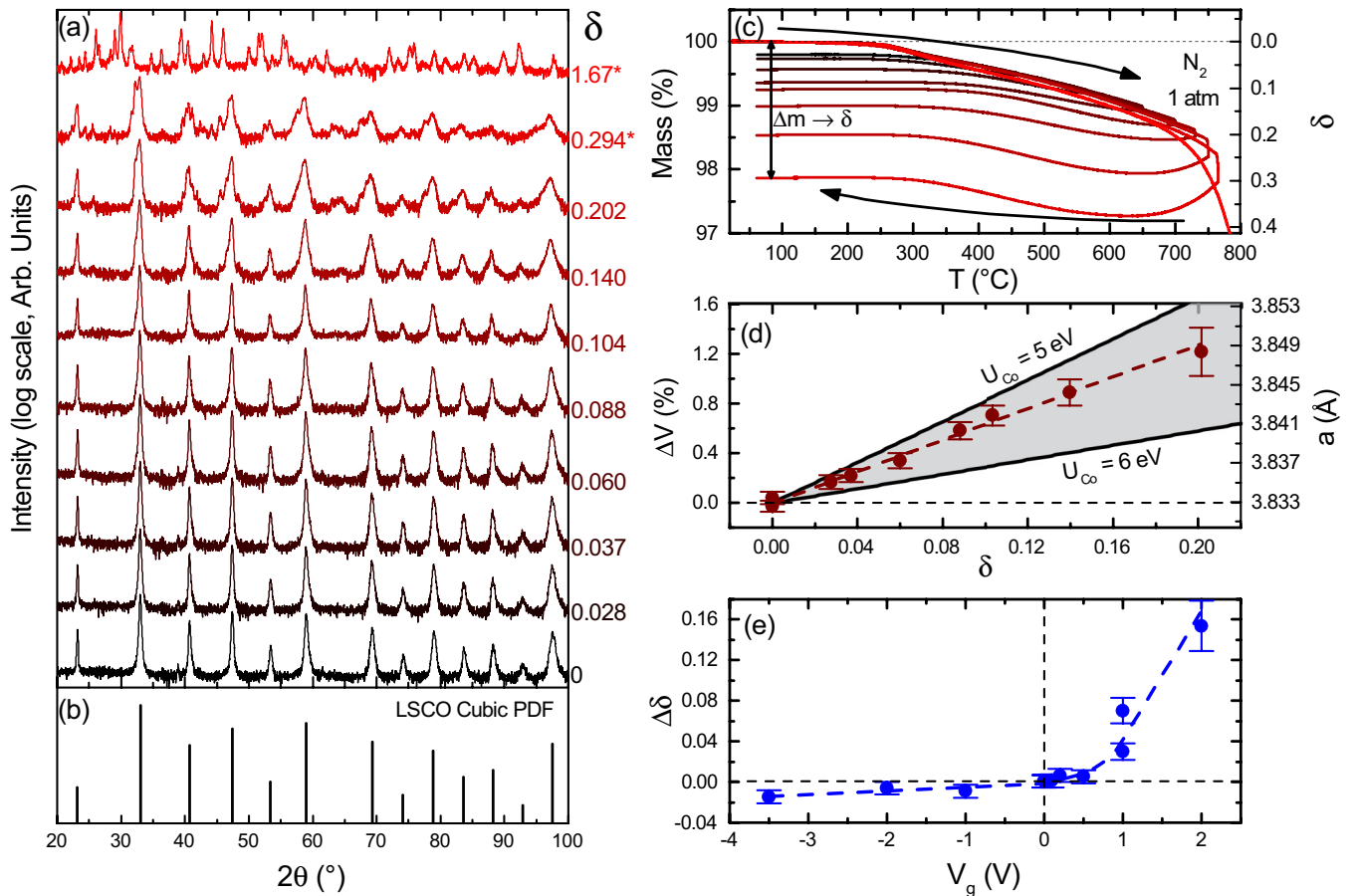


FIG. 2. (a) Powder x-ray diffraction patterns of *bulk*  $\text{La}_{0.5}\text{Sr}_{0.5}\text{CoO}_{3-\delta}$  before and after the thermogravimetric analysis (TGA) scans shown in (c), which induce progressive reduction. The  $\delta$  values from TGA are labeled on the right side of (a), and the curves are color-coordinated with (c). \* denotes samples no longer in the perovskite structure, which are omitted from further analysis. (b) Reference powder diffraction pattern for cubic  $\text{La}_{0.5}\text{Sr}_{0.5}\text{CoO}_3$ . (c) *Bulk* TGA scans, i.e., sample mass change (left axis) and conversion to  $\delta$  (right axis) vs temperature, for reduction in flowing  $\text{N}_2$ . (d) Change in bulk cell volume ( $\Delta V$ ) and bulk lattice parameter ( $a$ ) as a function of  $\delta$ . The maroon dotted line is a straight line fit and the solid black lines are the theoretical  $\Delta V$  due to formation of oxygen vacancies ( $U_{Co} = 5$  and  $6$  eV). (e) Change in  $\delta$  ( $\Delta\delta$ ) with  $V_g$  in *epitaxial films*, obtained by combining Figs. 1(c) and 2(d). The blue dashed line is a guide to the eye.

at negative bias [22].  $V_O$  formation is thus an obvious possibility for the positive-bias-induced lattice expansion in Fig. 1(c). To investigate the cell volume– $V_O$  density relationship in LSCO, *bulk* samples were systematically reduced in a TGA apparatus in flowing  $N_2$ . After each reduction these samples were then studied by PXRD. The PXRD pattern of the initial LSCO [bottom of Fig. 2(a)] is consistent with expectations for  $Pm\bar{3}m$  LSCO [Fig. 2(b)] [41]. As justified by the synthesis conditions and measured magnetic properties (Supplemental Material Sec. D [35]), we label this sample “ $\delta = 0$ ” in Fig. 2(a), i.e., we assume an initial state with negligible  $V_O$  density. The progressive reduction cycles shown in Fig. 2(c), to maximum temperatures from 340°C to 1000°C, result in mass loss that can be directly converted to  $\delta$ . The PXRD patterns in Fig. 2(a) are thereby labeled with a deduced  $\delta$ , increasing toward the top. The cubic perovskite structure is retained up to  $\delta = 0.202$ , above which secondary phases form, being LSCO reduction products (brownmillerite, binary oxides, etc.).

As shown in Fig. 2(d), which plots the cubic lattice parameter ( $a$ ) and cell volume expansion ( $\Delta V$ ) vs  $\delta$ , the reduction of bulk LSCO is indeed accompanied by lattice expansion, qualitatively consistent with prior work [42–44].  $\Delta V$  increases linearly with  $V_O$  concentration, at a rate that can be reproduced by DFT. Specifically, as detailed in Supplemental Material Sec. E (Fig. S3, Table S1) [32] incorporation of  $V_O$ 's in DFT supercells at various concentrations results in the solid lines shown in Fig. 2(d) for Co  $U$  values ( $U_{Co}$ ) of 5 and 6 eV. A  $U_{Co}$  between these values, which is reasonable for Co perovskites [45], thus quantitatively reproduces the experimental  $\Delta V(\delta)$ . Taken with the earlier indirect conclusion of  $V_O$  formation from transport, and the observation of irreversibility in vacuum that is suppressed in  $O_2$  (Supplemental Material Sec. F [32]), we take these results as strong evidence for  $V_O$  formation as the source of lattice expansion at positive  $V_g$  in Fig. 1(c). Importantly, this  $\Delta V(\delta)$  relationship for bulk LSCO can then be used in conjunction with the  $\Delta V(V_g)$  relationship for gated films to quantitatively estimate the change in  $\delta$  induced by  $V_g$ . This essentially uses the bulk data of Fig. 2(d) as a calibration to quantify  $\delta(V_g)$  from Fig. 1(c), assuming the cell expansion with  $\delta$  to be similar in films and bulk. The straight line fit in Fig. 2(d) was used for this purpose, resulting in Fig. 2(e). Here, we simply plot  $\Delta\delta$ , the  $V_g$ -induced change in  $\delta$  with respect to zero bias, as the initial  $\delta$  in these films is not accurately known [46]. [As outlined in Supplemental Material Sec. G (Fig. S5) [32], the Poisson ratio can also be accounted for in this analysis, assuming isotropic linear elasticity; this modifies the absolute values in Fig. 2(e) but not the qualitative trend.] The resulting induced  $\delta$ 's at positive  $V_g$  are large but reasonable, reaching 0.16 at 2 V. Note here that (a)  $\delta < 0.5$  even at the largest positive  $V_g$  is consistent with the absence of brownmillerite in SXRD, and (b) strong arguments can be made against a H incorporation mechanism (Supplemental Material Sec. H [32]). While the interpretation of the large structural changes at  $V_g > 0$  are thus clear, the small ones occurring at  $V_g < 0$  could involve both electrochemistry and electrostatics (Supplemental Material Sec. I, Table S2 [32]).

Clearly, a key conclusion from the above is that bias-induced  $V_O$ 's appear to penetrate the entire film thickness. To verify this, a depth-sensitive technique, neutron reflectometry, was applied. Although  $V_O$  formation at the densities in

Fig. 2(e) results in nuclear scattering length density changes that are difficult to discern [Supplemental Material Sec. J (Tables S3 and S4) [32]], the subsequent impact on magnetization is substantial. Magnetization depth profiling via PNR was thus performed, using devices scaled to  $10 \times 5 \text{ mm}^2$  LSCO channels [Fig. 3(a)]. Figure 3(b) shows the scattering vector ( $Q$ ) dependence of the specular neutron reflectivity for 42-unit-cell-thick LSCO, at 30 K in a 3 T in-plane field [47] at  $V_g = 0$ . The non-spin-flip reflectivities (“ $R^{++}$ ” and “ $R^{--}$ ”) are shown, where “+” and “−” indicate the polarization of the incoming and outgoing beams [Fig. 3(a)]. As expected, well below  $T_C$  in a large in-plane field,  $R^{++}$  and  $R^{--}$  are clearly split. Figure 3(c) plots the spin asymmetry,  $SA = \frac{R^{++} - R^{--}}{R^{++} + R^{--}}$ , which, in the absence of large  $V_g$ -dependent chemical changes, highlights the magnetic scattering. This SA is positive, with two oscillations visible to the maximum  $Q$ . Most significantly, Figs. 3(d) and 3(e) show that the SA responds dramatically to  $V_g$ . The SA is reduced substantially at 2 V, but with a similar oscillation period, while at 3 V the SA appears completely suppressed. Even prior to quantitative analysis, this SA reduction with  $V_g$  indicates strong suppression of the magnetization, the similarity of the period in Figs. 3(c) and 3(d) indicating little change in magnetic thickness, i.e., relatively uniform suppression.

Quantitative refinement was performed to substantiate these conclusions, resulting in the solid line fits in Figs. 3(b)–3(e). As discussed in Supplemental Material Sec. J [32], these fits are based on a model including the LAO substrate, LSCO film, and ion gel. The refined nuclear scattering length density for LSCO is as expected, and independent of  $V_g$  (along with the chemical thickness). Note here that varying  $\delta$  between  $\text{La}_{0.5}\text{Sr}_{0.5}\text{CoO}_3$  and  $\text{La}_{0.5}\text{Sr}_{0.5}\text{CoO}_{2.84}$  [as in Fig. 2(e)] results in nuclear scattering length density changes of only 3%, confirming little sensitivity to this effect. The depth-dependent magnetization [ $M(z)$ ], however, is highly sensitive to  $V_O$  density. The refined  $M(z)$  from Figs. 3(b)–3(e) is plotted in Fig. 3(f). At  $V_g = 0$  a single ferromagnetic LSCO layer with  $M = 1.68\mu_B/\text{Co}$  describes the data [Figs. 3(b) and 3(c)], with roughnesses of 4 and 8 Å at the LAO/LSCO and LSCO/ion-gel interfaces, respectively.  $1.68\mu_B/\text{Co}$  is slightly lower than the bulk saturation magnetization ( $1.9\mu_B/\text{Co}$ ), but is consistent with magnetometry on these films [47]. While a reasonable description of the 2 and 3 V data was also possible with a single ferromagnetic LSCO layer with progressively suppressed  $M$ , statistically significant fit improvements were obtained by introducing a second layer. This captures the weak dip to negative SA around  $0.045 \text{ \AA}^{-1}$  in Fig. 3(d). The resulting  $M(z)$  in Fig. 3(f) reveals strong suppression of  $M$  with increasing  $V_g$ . At 2 V,  $M$  is roughly cut in half, the region closest to the ion-gel interface having a slightly stronger reduction than the bulk of the film. At 3 V,  $M$  then becomes very small, a weakly magnetized bottom section of the LSCO providing the fit in Fig. 3(e). These results not only confirm near-uniform magnetization suppression, but are also *quantitatively* consistent with the  $\delta$ 's from SXRD. Explicitly, taking the depth-averaged  $M(V_g)$  from Fig. 3(f), and using bulk data for the  $x$  dependence of saturation magnetization in  $\text{La}_{1-x}\text{Sr}_x\text{CoO}_3$  [48], an effective doping level ( $x_{\text{eff}}$ ) can be extracted at each  $V_g$ . Using the fact that Sr hole doping is

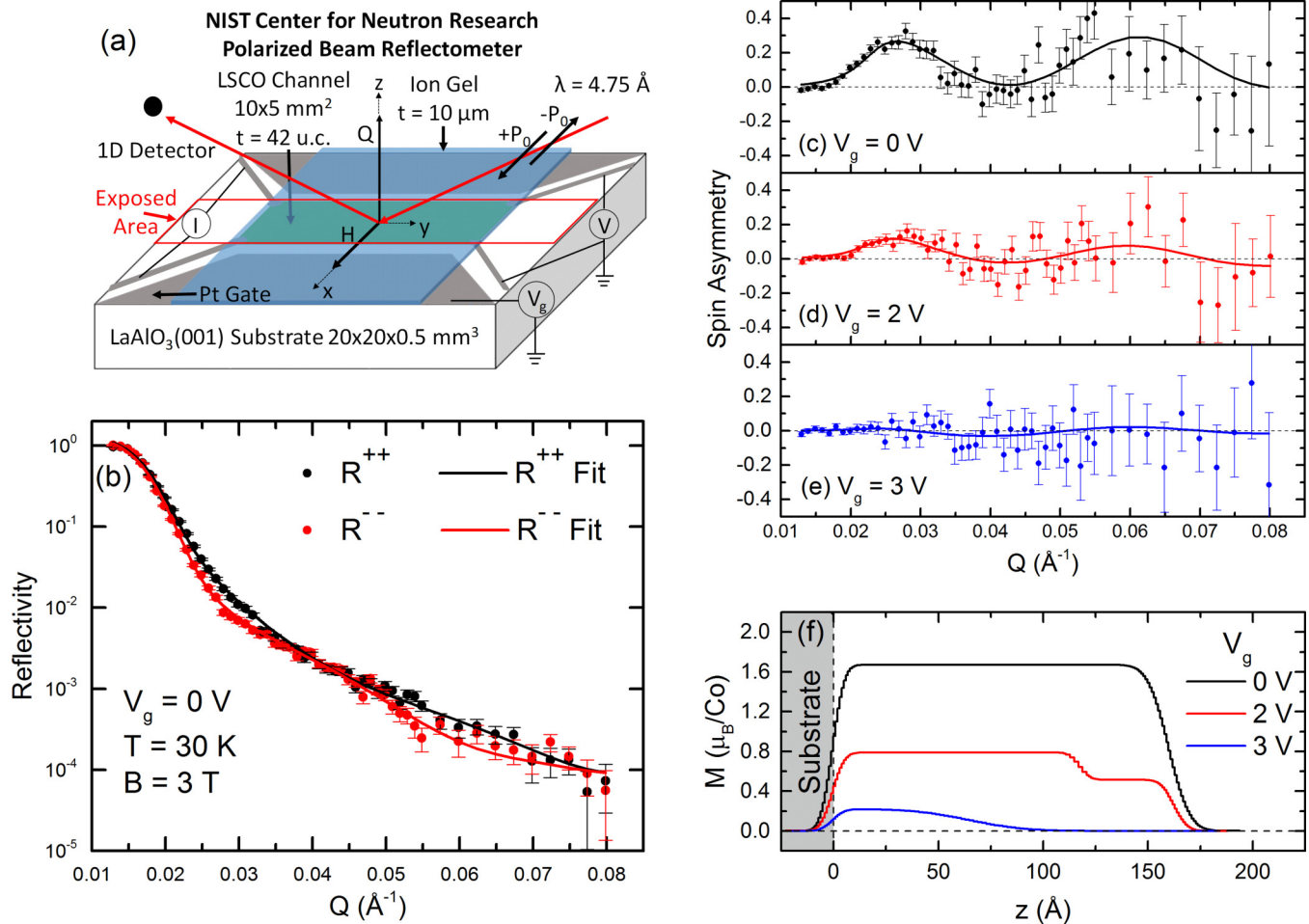


FIG. 3. (a) Device and experimental setup schematic for polarized neutron reflectometry on epitaxial  $\text{La}_{0.5}\text{Sr}_{0.5}\text{CoO}_{3-\delta}$  films. (b) Reflectivity ( $R$ ) vs scattering vector magnitude,  $Q$ , from a  $165 \text{ \AA}$  film at zero gate bias ( $V_g$ ),  $30 \text{ K}$ , and  $3 \text{ T}$ . Black and red denote the non-spin-flip “ $R^{++}$ ” and “ $R^{--}$ ” channels, respectively, for both data (points) and the fits to the model discussed in the text (lines). (c)–(e) Spin asymmetry at  $30 \text{ K}$  in  $3 \text{ T}$  for  $V_g = 0, 2, \text{ and } 3 \text{ V}$ , respectively. Solid lines are fits to the model discussed in the text. (f) Extracted magnetization ( $M$ ) depth profile at  $30 \text{ K}$  in  $3 \text{ T}$  for  $V_g = 0, 2, \text{ and } 3 \text{ V}$ ;  $z = 0$  is the substrate/film interface.

compensated by  $V_{\text{O}}$ 's according to  $x_{\text{eff}} = x - 2\delta$  (assuming doubly ionized  $V_{\text{O}}$  donors), the curves in Fig. 3(f) can then be associated with an induced  $\delta$ . These values are  $0.11$  and  $0.18$  for  $V_g = 2$  and  $3 \text{ V}$ , which, considering the approximations, are in reasonable agreement with Fig. 2(e). While this analysis ignores other factors in the relationship between  $M$  and  $\delta$ , making it only approximate, such an approach has been employed before and independently verified [34].

Given that the electric field in EDLTs based on metallic perovskites should be screened over quite short scales (the Thomas-Fermi screening length is a few unit cells) the observation of gate-induced  $V_{\text{O}}$  formation through 40-unit-cell films warrants discussion. One interpretation is that  $V_{\text{O}}$  creation is first achieved by the EDL electric field at the extreme surface of LSCO. While the details remain to be understood, this would then generate an O chemical potential gradient, driving further out-migration of O from the bulk, potentially assisted by the electric field. Importantly, the  $V_{\text{O}}$  diffusivity in LSCO [49] is large enough to support this interpretation, translating to a  $V_{\text{O}}$  diffusion length of  $35 \text{ nm}$  at  $300 \text{ K}$  on the time scales used here, well in excess of the  $17 \text{ nm}$  film thickness. The enthalpy

of formation of  $V_{\text{O}}$ 's is also low in LSCO (as utilized in recent Gd gettering studies [50]) due to the instability of  $\text{Co}^{4+}$  formal valence. This results in extraordinary redox activity at  $x = 1$ , consistent with recent demonstrations of thermal [51] and electrolyte-assisted [28] switching between  $\text{SrCoO}_{3-\delta}$  and brownmillerite  $\text{SrCoO}_{2.5}$ . The extent to which EDLT response in a given system involves redox is thus heavily influenced by the enthalpy of formation of  $V_{\text{O}}$ 's, their diffusivity, and the  $V_g$  polarity.

In summary, we report the use of SXR and PNR as *in operando* probes of gating mechanisms in ion-gel-based LSCO EDLTs. Large positive-bias-induced lattice expansion is observed, providing direct evidence of  $V_{\text{O}}$  formation. Complementary bulk measurements using TGA and PXR, supported by DFT, are then used to quantify the  $V_g$ -dependent  $V_{\text{O}}$  density, which reaches  $\delta = 0.16$  at  $+2 \text{ V}$ . This electrochemical reduction penetrates the entire thickness of  $\sim 30$ -unit-cell-thick films, confirmed by uniform suppression of the magnetization depth profile from PNR, quantitatively consistent with the deduced  $V_{\text{O}}$  density. The results thus establish SXR and PNR as powerful *in operando* probes of electrolyte-gated

materials, significantly advancing our understanding of gating mechanisms in oxide EDLTs.

This work was primarily supported by the National Science Foundation through the UMN MRSEC under DMR-1420013. This work was partially supported (specifically the neutron scattering component) by the DOE through the UMN Center

for Quantum Materials, under DE-FG02-06ER46275 and DE-SC-0016371. Parts of this work were carried out in the Characterization Facility, UMN, which receives partial support from NSF through the MRSEC program. This research used resources of the Advanced Photon Source, a DOE Office of Science User Facility operated by Argonne National Laboratory under Contract No. DE-AC02-06CH11357.

- 
- [1] C. H. Ahn, A. Bhattacharya, M. Di Ventra, J. N. Eckstein, C. D. Frisbie, M. E. Gershenson, A. M. Goldman, I. H. Inoue, J. Mannhart, A. J. Millis, A. F. Morpurgo, D. Natelson, and J.-M. Triscone, Electrostatic modification of novel materials, *Rev. Mod. Phys.* **78**, 1185 (2006).
- [2] A. M. Goldman, Electrostatic gating of ultrathin films, *Annu. Rev. Mater. Res.* **44**, 45 (2014).
- [3] K. H. Lee, M. S. Kang, S. Zhang, Y. Gu, T. P. Lodge, and C. D. Frisbie, “Cut and stick” rubbery ion gels as high capacitance gate dielectrics, *Adv. Mater.* **24**, 4457 (2012).
- [4] W. Xie, X. Zhang, C. Leighton, and C. D. Frisbie, 2D insulator-metal transition in aerosol-jet-printed electrolyte-gated indium oxide thin film transistors, *Adv. Electron. Mater.* **3**, 1600369 (2017).
- [5] H. Yuan, H. Shimotani, A. Tsukazaki, A. Ohtomo, M. Kawasaki, and Y. Iwasa, High-density carrier accumulation in ZnO field-effect transistors gated by electric double layers of ionic liquids, *Adv. Funct. Mater.* **19**, 1046 (2009).
- [6] K. Ueno, S. Nakamura, H. Shimotani, H. T. Yuan, N. Kimura, T. Nojima, H. Aoki, Y. Iwasa, and M. Kawasaki, Discovery of superconductivity in  $\text{KTaO}_3$  by electrostatic carrier doping, *Nat. Nanotechnol.* **6**, 408 (2011).
- [7] R. Scherwitzl, P. Zubko, I. G. Lezama, S. Ono, A. F. Morpurgo, G. Catalan, and J. M. Triscone, Electric-field control of the metal-insulator transition in ultrathin  $\text{NdNiO}_3$  films, *Adv. Mater.* **22**, 5517 (2010).
- [8] Y. Yamada, K. Ueno, T. Fukumura, H. T. Yuan, H. Shimotani, Y. Iwasa, L. Gu, S. Tsukimoto, Y. Ikuhara, and M. Kawasaki, Electrically induced ferromagnetism at room temperature in cobalt-doped titanium dioxide, *Science* **332**, 1065 (2011).
- [9] A. S. Dhoot, C. Israel, X. Moya, N. D. Mathur, and R. H. Friend, Large Electric Field Effect in Electrolyte-Gated Manganites, *Phys. Rev. Lett.* **102**, 136402 (2009).
- [10] K. Ueno, S. Nakamura, H. Shimotani, A. Ohtomo, N. Kimura, T. Nojima, H. Aoki, Y. Iwasa, and M. Kawasaki, Electric-field-induced superconductivity in an insulator, *Nat. Mater.* **7**, 855 (2008).
- [11] A. T. Bollinger, G. Dubuis, J. Yoon, D. Pavuna, J. Misewich, and I. Božović, Superconductor-insulator transition in  $\text{La}_{2-x}\text{Sr}_x\text{CuO}_4$  at the pair quantum resistance, *Nature (London)* **472**, 458 (2011).
- [12] X. Leng, J. Garcia-Barriocanal, S. Bose, Y. Lee, and A. M. Goldman, Electrostatic Control of the Evolution from a Superconducting Phase to an Insulating Phase in Ultrathin  $\text{YBa}_2\text{Cu}_3\text{O}_{7-x}$  Films, *Phys. Rev. Lett.* **107**, 027001 (2011).
- [13] J. Ye, Y. Zhang, R. Akashi, and M. Bahramy, Superconducting dome in a gate-tuned band insulator, *Science* **338**, 1193 (2012).
- [14] M. Nakano, K. Shibuya, D. Okuyama, T. Hatano, S. Ono, M. Kawasaki, Y. Iwasa, and Y. Tokura, Collective bulk carrier delocalization driven by electrostatic surface charge accumulation, *Nature (London)* **487**, 459 (2012).
- [15] S. Asanuma, P.-H. Xiang, H. Yamada, H. Sato, I. H. Inoue, H. Akoh, A. Sawa, K. Ueno, H. Shimotani, H. Yuan, M. Kawasaki, and Y. Iwasa, Tuning of the metal-insulator transition in electrolyte-gated  $\text{NdNiO}_3$  thin films, *Appl. Phys. Lett.* **97**, 142110 (2010).
- [16] S. Wang, M. Ha, M. Manno, C. D. Frisbie, and C. Leighton, Hopping transport and the Hall effect near the insulator-metal transition in electrochemically gated poly(3-hexylthiophene) transistors, *Nat. Commun.* **3**, 1210 (2012).
- [17] W. Xie, S. Wang, X. Zhang, C. Leighton, and C. D. Frisbie, High Conductance 2D Transport Around the Hall Mobility Peak in Electrolyte-Gated Rubrene Crystals, *Phys. Rev. Lett.* **113**, 246602 (2014).
- [18] J. Ye, M. F. Craciun, M. Koshino, S. Russo, S. Inoue, H. Yuan, H. Shimotani, A. F. Morpurgo, and Y. Iwasa, Accessing the transport properties of graphene and its multilayers at high carrier density, *Proc. Natl. Acad. Sci. USA* **108**, 13002 (2011).
- [19] T. Yamaguchi, E. Watanabe, H. Osato, D. Tsuya, K. Deguchi, T. Watanabe, H. Takeya, Y. Takano, S. Kurihara, and H. Kawarada, Low-temperature transport properties of holes introduced by ionic liquid gating in hydrogen-terminated diamond surfaces, *J. Phys. Soc. Jpn.* **82**, 74718 (2013).
- [20] H. Ji, J. Wei, and D. Natelson, Modulation of the electrical properties of  $\text{VO}_2$  nanobeams using an ionic liquid as a gating medium, *Nano Lett.* **12**, 2988 (2012).
- [21] Z. Yang, Y. Zhou, and S. Ramanathan, Studies on room-temperature electric-field effect in ionic-liquid gated  $\text{VO}_2$  three-terminal devices, *J. Appl. Phys.* **111**, 14506 (2012).
- [22] J. Walter, H. Wang, B. Luo, C. D. Frisbie, and C. Leighton, Electrostatic versus electrochemical doping and control of ferromagnetism in ion-gel-gated ultrathin  $\text{La}_{0.5}\text{Sr}_{0.5}\text{CoO}_{3-\delta}$ , *ACS Nano* **10**, 7799 (2016).
- [23] J. Jeong, N. Aetukuri, T. Graf, T. D. Schladt, M. G. Samant, and S. S. P. Parkin, Suppression of metal-insulator transition in  $\text{VO}_2$  by electric field-induced oxygen vacancy formation, *Science* **339**, 1402 (2013).
- [24] M. Li, W. Han, X. Jiang, J. Jeong, M. G. Samant, and S. S. P. Parkin, Suppression of ionic liquid gate-induced metallization of  $\text{SrTiO}_3(001)$  by oxygen, *Nano Lett.* **13**, 4675 (2013).
- [25] T. D. Schladt, T. Graf, N. B. Aetukuri, M. Li, A. Fantini, X. Jiang, M. G. Samant, and S. S. P. Parkin, Crystal-facet-dependent metallization in electrolyte-gated rutile  $\text{TiO}_2$  single crystals, *ACS Nano* **7**, 8074 (2013).
- [26] D. Okuyama, M. Nakano, S. Takeshita, H. Ohsumi, S. Tardif, K. Shibuya, T. Hatano, H. Yumoto, T. Koyama, H. Ohashi,

- M. Takata, M. Kawasaki, T. Arima, Y. Tokura, and Y. Iwasa, Gate-tunable gigantic lattice deformation in  $\text{VO}_2$ , *Appl. Phys. Lett.* **104**, 23507 (2014).
- [27] X. Leng, J. Pereiro, J. Strle, G. Dubuis, A. T. Bollinger, A. Gozar, J. Wu, N. Litombe, C. Panagopoulos, D. Pavuna, and I. Božović, Insulator to metal transition in  $\text{WO}_3$  induced by electrolyte gating, *Quantum Mater.* **2**, 35 (2017).
- [28] N. Lu, P. Zhang, Q. Zhang, R. Qiao, Q. He, H.-B. Li, Y. Wang, J. Guo, D. Zhang, Z. Duan, Z. Li, M. Wang, S. Yang, M. Yan, E. Arenholz, S. Zhou, W. Yang, L. Gu, C.-W. Nan, J. Wu, Y. Tokura, and P. Yu, Electric-field control of tri-state phase transformation with a selective dual-ion switch, *Nature (London)* **546**, 124 (2017).
- [29] G. Dubuis, Y. Yacoby, H. Zhou, X. He, A. T. Bollinger, D. Pavuna, R. Pindak, and I. Božović, Oxygen displacement in cuprates under ionic liquid field-effect gating, *Sci. Rep.* **6**, 32378 (2016).
- [30] Y. Dong, H. Xu, Z. Luo, H. Zhou, D. D. Fong, W. Wu, and C. Gao, Effect of gate voltage polarity on the ionic liquid gating behavior of  $\text{NdNiO}_3/\text{NdGaO}_3$  heterostructures, *APL Mater.* **5**, 51101 (2017).
- [31] A. M. Perez-Muñoz, P. Schio, R. Poloni, A. Fernandez-Martinez, A. Rivera-Calzada, J. C. Cezar, E. Salas-Colera, G. R. Castro, J. Kinney, C. Leon, J. Santamaria, J. Garcia-Barriocanal, and A. M. Goldman, *In operando* evidence of deoxygenation in ionic liquid gating of  $\text{YBa}_2\text{Cu}_3\text{O}_{7-x}$ , *Proc. Natl. Acad. Sci. U.S.A.* **114**, 215 (2017).
- [32] See Supplemental Material at <http://link.aps.org/supplemental/10.1103/PhysRevMaterials.1.071403> for additional information on film growth, device fabrication, *in operando* measurements, and complementary bulk measurements/calculations.
- [33] M. A. Torija, M. Sharma, M. R. Fitzsimmons, M. Varela, and C. Leighton, Epitaxial  $\text{La}_{0.5}\text{Sr}_{0.5}\text{CoO}_3$  thin films: Structure, magnetism, and transport, *J. Appl. Phys.* **104**, 023901 (2008).
- [34] M. A. Torija, M. Sharma, J. Gazquez, M. Varela, C. He, J. Schmitt, J. A. Borchers, M. Laver, S. El-Khatib, and C. Leighton, Chemically driven nanoscopic magnetic phase separation at the  $\text{SrTiO}_3(001)/\text{La}_{1-x}\text{Sr}_x\text{CoO}_3$  interface, *Adv. Mater.* **23**, 2711 (2011).
- [35] J. Gazquez, S. Bose, M. Sharma, M. A. Torija, S. J. Pennycook, C. Leighton, and M. Varela, Lattice mismatch accommodation via oxygen vacancy ordering in epitaxial  $\text{La}_{0.5}\text{Sr}_{0.5}\text{CoO}_{3-\delta}$  thin films, *APL Mater.* **1**, 12105 (2013).
- [36] S. Kelly, F. Galli, J. Aarts, S. Bose, M. Sharma, and C. Leighton, Direct real space observation of magneto-electronic inhomogeneity in ultra-thin film  $\text{La}_{0.5}\text{Sr}_{0.5}\text{CoO}_{3-\delta}$  on  $\text{SrTiO}_3(001)$ , *Appl. Phys. Lett.* **105**, 112909 (2014).
- [37] B. J. Kirby, P. A. Kienzle, B. B. Maranville, N. F. Berk, J. Krycka, F. Heinrich, and C. F. Majkrzak, Phase-sensitive specular neutron reflectometry for imaging the nanometer scale composition depth profile of thin-film materials, *Curr. Opin. Colloid Interface Sci.* **17**, 44 (2012).
- [38] G. Kresse and J. Hafner, *Ab initio* molecular dynamics for liquid metals, *Phys. Rev. B* **47**, 558 (1993).
- [39] G. Kresse and J. Furthmüller, Efficient iterative schemes for *ab initio* total-energy calculations using a plane-wave basis set, *Phys. Rev. B* **54**, 11169 (1996).
- [40] X. Wu, J. Walter, T. Feng, J. Zhu, H. Zheng, J. F. Mitchell, N. Biškup, M. Varela, X. Ruan, C. Leighton, and X. Wang, Glass-like thermal conductivity induced by oxygen vacancies in nanoscale epitaxial  $\text{La}_{0.5}\text{Sr}_{0.5}\text{CoO}_{3-\delta}$ , *Adv. Funct. Mater.* **27**, 1704233 (2017).
- [41] Note here that a crossover from  $R\bar{3}c$  to  $Pm\bar{3}m$  occurs around  $x = 0.5$  in LSCO. While minor deviations from cubic are thus possible, we simply analyze all data here in terms of the cubic structure.
- [42] R. P. Haggerty and R. Seshadri, Oxygen stoichiometry, crystal structure, and magnetism of  $\text{La}_{0.5}\text{Sr}_{0.5}\text{CoO}_3$ , *J. Phys.: Condens. Matter* **16**, 6477 (2004).
- [43] J. Mizusaki, Y. Mima, S. Yamauchi, and K. Fueki, Nonstoichiometry of the perovskite-type oxides  $\text{La}_{1-x}\text{Sr}_x\text{CoO}_{3-\delta}$ , *J. Solid State Chem.* **80**, 102 (1989).
- [44] A. Ringuedé and J. Fouletier, Oxygen reaction on strontium-doped lanthanum cobaltite dense electrodes at intermediate temperatures, *Solid State Ionics* **139**, 167 (2001).
- [45] H. Hsu, P. Blaha, R. M. Wentzcovitch, and C. Leighton, Cobalt spin states and hyperfine interactions in  $\text{LaCoO}_3$  investigated by LDA+ $U$ , *Phys. Rev. B* **82**, 100406 (2010).
- [46] This value has been estimated in our prior work [40] to lie around 0.09 for similar films grown on LAO.
- [47] As reported earlier [22], LAO(001)/LSCO films exhibit strong perpendicular magnetic anisotropy. A large (3 T) in-plane magnetic field was thus required to achieve the in-plane alignment necessary for PNR in the geometry shown in Fig. 3(a).
- [48] J. Wu and C. Leighton, Glassy ferromagnetism and magnetic phase separation in  $\text{La}_{1-x}\text{Sr}_x\text{CoO}_3$ , *Phys. Rev. B* **67**, 174408 (2003).
- [49] R. De Souza, Oxygen transport in  $\text{La}_{1-x}\text{Sr}_x\text{Mn}_{1-y}\text{Co}_y\text{O}_{3\pm\delta}$  perovskites: Part I. Oxygen tracer diffusion, *Solid State Ionics* **106**, 175 (1998).
- [50] D. A. Gilbert, A. J. Grutter, P. Murray, R. V. Chopdekar, A. M. Kane, A. L. Ionin, S. R. Spurgeon, B. J. Kirby, B. B. Maranville, A. T. N'Diaye, A. Mehta, E. Arenholz, K. Liu, Y. Takamura, and J. A. Borchers, Ionic tuning of cobaltites at the nanoscale (unpublished).
- [51] H. Jeen, W. S. Choi, M. D. Biegalski, C. M. Folkman, I.-C. Tung, D. D. Fong, J. W. Freeland, D. Shin, H. Ohta, M. F. Chisholm, and H. N. Lee, Reversible redox reactions in an epitaxially stabilized  $\text{SrCoO}_x$  oxygen sponge, *Nat. Mater.* **12**, 1057 (2013).